# Supplemental Material for "Generalized Gradient Approximation Made Thermal"

John Kozlowski and Dennis Perchak

*Department of Chemistry, University of California, Irvine, CA 92697, USA*

Kieron Burke

*Department of Chemistry, University of California, Irvine, CA 92697, USA and*
*Department of Physics and Astronomy, University of California, Irvine, CA 92697, USA*

(Dated: August 8, 2023)

Below we provide supplemental figures accompanying the main text, including various plots depicting the accuracy of the locally-thermal Perdew–Burke–Ernzerhof (ltPBE) ansatz relative to conditional-probability density functional theory (CP-DFT) data, and its satisfaction of two exact conditions. When useful, we make comparisons to other thermal generalized gradient approximations in the literature, namely the one proposed by Karasiev *et al.* (referred to here as KDT16).

## CONTENTS

## 1.  CP-DFT RESULTS

### 1.1.  XC Enhancement Factors

All CP-DFT XC enhancement factor data has been included as .csv files for systems of various densities, gradients, and temperatures. We include files for unpolarized systems: $r_{\rm s} = 0.1, 0.5, 1, 2, 4, 10$ for $0 \leq s \leq 5$ and $0.05 \leq t \leq 4$; and for fully polarized systems: $r_{\rm s} = 0.1, 0.5, 1, 2, 4$ for $0 \leq s \leq 3$ and $0.05 \leq t \leq 4$.

The ltPBE approximation is depicted alongside CP-DFT data in the following figures, showing its performance for each density at select reduced temperatures. Fig. S1 depicts the results for unpolarized data, while Fig. S2 depicts the results for fully polarized data.

### 1.2.  XC Hole Densities

Below we depict various plots illustrating the temperature-dependent XC hole densities output from the CP-DFT procedure outlined in the main text. Fig. S3 depicts the results for unpolarized systems, while Fig. S4 depicts the results for fully polarized systems. In all cases, the CP-DFT procedure produces an XC hole density with the same on-top value and energy as PBE as $t \to 0$.
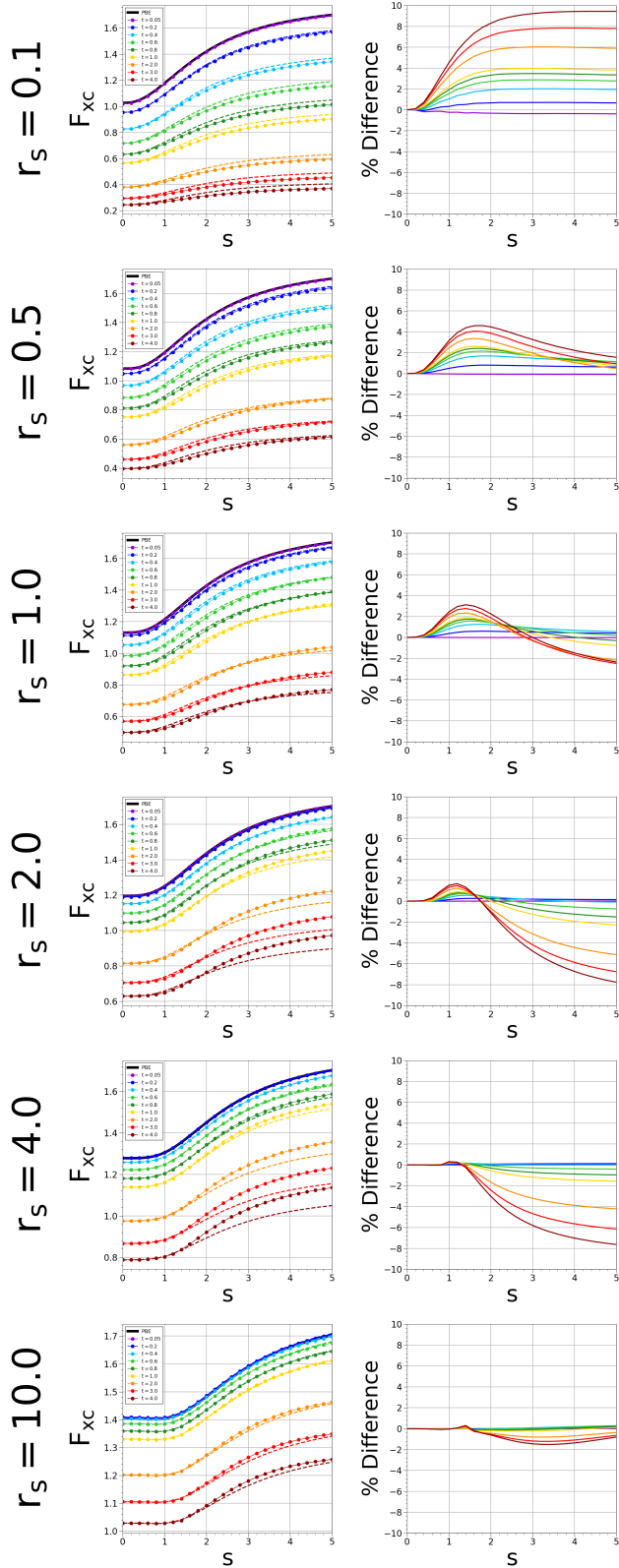
FIG. S1. Grid of plots depicting temperature-dependent XC enhancement factors as functions of the dimensionless gradient $s$ for unpolarized systems of various $r_S$ values. The data points represent CP-DFT calculations connected by solid lines, while the ltPBE approximation (Eq. 1) is represented by the dashed curves. The corresponding percent deviation of the ltPBE ansatz is included, largely found to be $\leq 8\%$ (but often much less) in the tested temperature range.
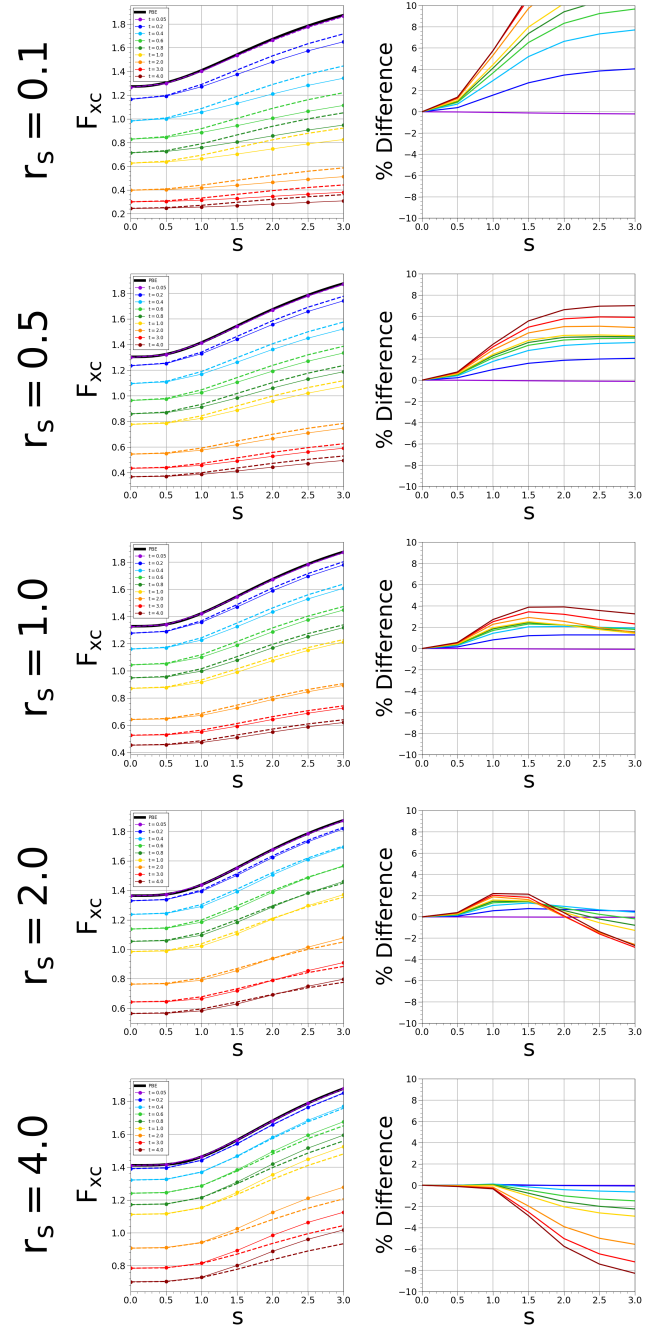
FIG. S2. Grid of plots depicting temperature-dependent XC enhancement factors as functions of the dimensionless gradient $s$ for fully polarized systems of various $r_S$ values. The data points represent CP-DFT calculations connected by solid lines, while the ltPBE approximation (Eq. 1) is represented by the dashed curves. The corresponding percent deviation of the ltPBE ansatz is included, largely found to be $\leq 8\%$ (but often much less) in the tested temperature range.
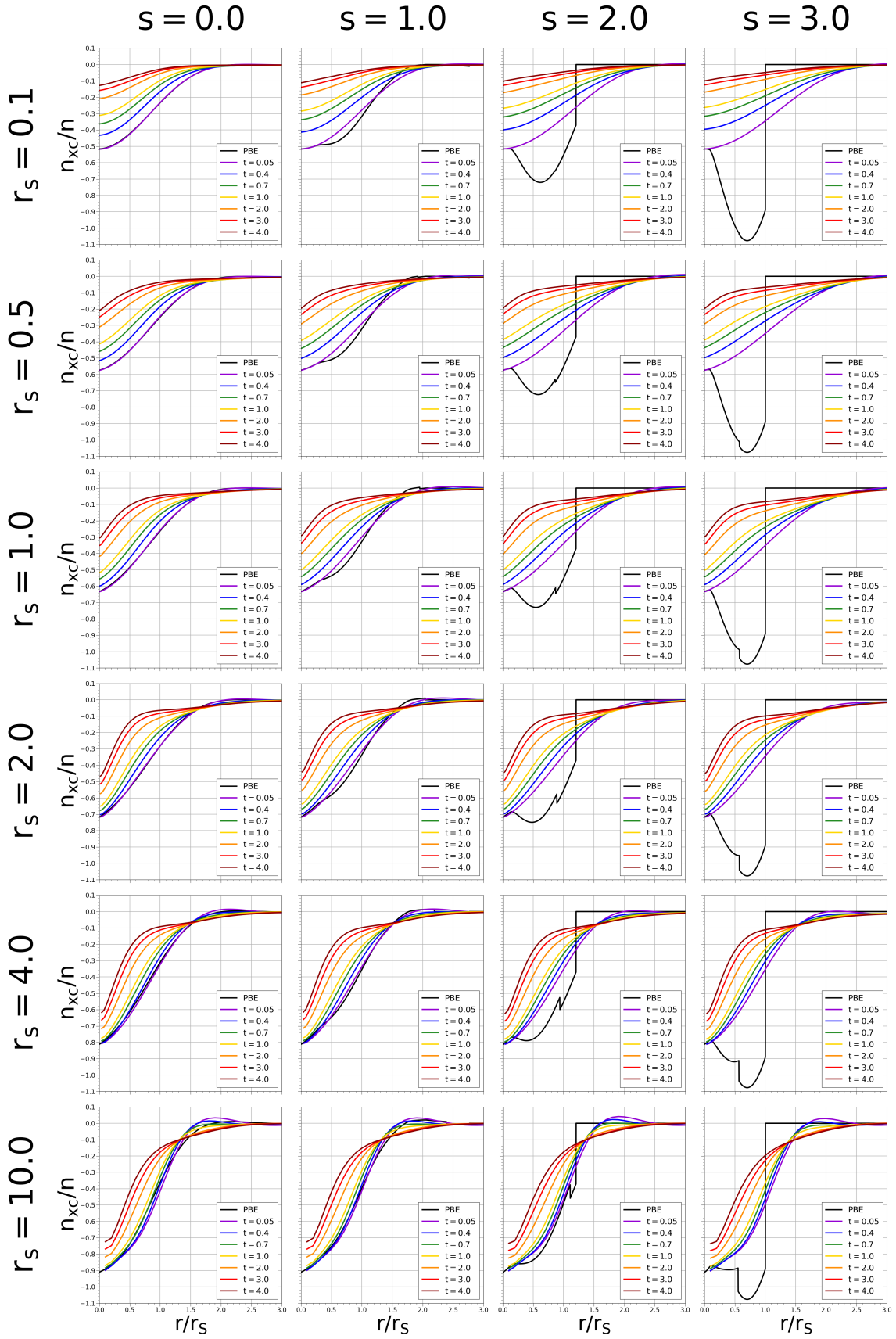
FIG. S3. Grid of plots depicting temperature-dependent XC hole densities for unpolarized systems of various $r_\mathrm{S}$, $s$, and $t$. We use black to denote the ground-state PBE XC hole density, while the CP-DFT XC hole at different reduced temperatures is depicted in various colors.

FIG. S4. Grid of plots depicting temperature-dependent XC hole densities for fully polarized systems of various $r_\mathrm{s}$, $s$, and $t$. We use black to denote the ground-state PBE XC hole density, while the CP-DFT XC hole at different reduced temperatures is depicted in various colors.
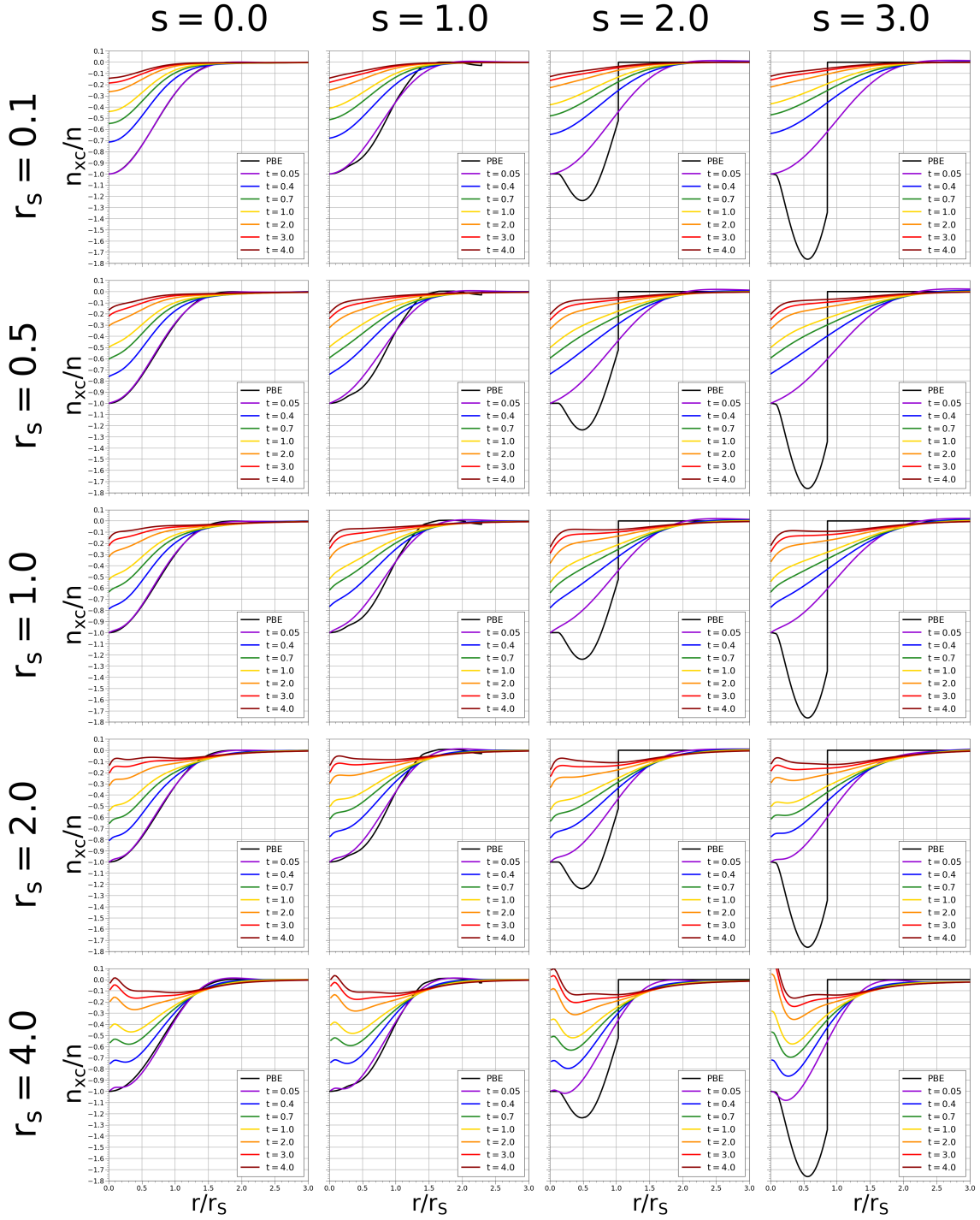
## 2.   EXACT CONDITIONS AT NONZERO TEMPERATURE

### 2.1.   Coordinate Scaling Inequality

Here we provide additional plots depicting the satisfaction of the thermal coordinate scaling inequality (Eq. 8 of the main text) by ltPBE, and violation by KDT16. In Fig. S5 we plot $F_{\mathrm{XC}}$ curves at fixed values of $t$ for ltPBE and KDT16, illustrating the differences between the two approximations. The ltPBE enhancement factor, having inherited the curvature of the ground-state $F_{\mathrm{XC}}^{\mathrm{PBE}}$, naturally satisfies this exact condition at all temperatures. In contrast the KDT16 approximation only satisfies this exact condition when $t \to 0$, where it recreates PBE, but violates it as the temperature is increased into the warm dense matter regime.

### 2.2.   Concavity Condition

Here we show various contour plots depicting the thermal concavity condition (Eq. 11 of the main text) for ltPBE and KDT16 at different $s$ values. Looking at Fig. S6, it is clear that the ltPBE approximation satisfies this condition, regardless of the value of $s$, due to its expression always being negative. It is also clear that KDT16 satisfies the concavity condition as $s \to 0$ (where it reduces to thermal LDA), but violates the condition as $s$ is increased. Noting that the density of a system scales according to $n_\gamma(\mathbf{r}) = \gamma^3 n(\gamma \mathbf{r})$, we observe violations for KDT16 for both moderate/high densities with nonzero $s$ in the warm dense matter regime.

FIG. S6.   Contours of the thermal concavity condition inequality (Eq. 11) with initial density $n = 1$. Here we show both the ltPBE (top) and KDT16 (bottom) approximations, confirming that the condition is satisfied by ltPBE, but is violated by KDT16 (red denotes positive).
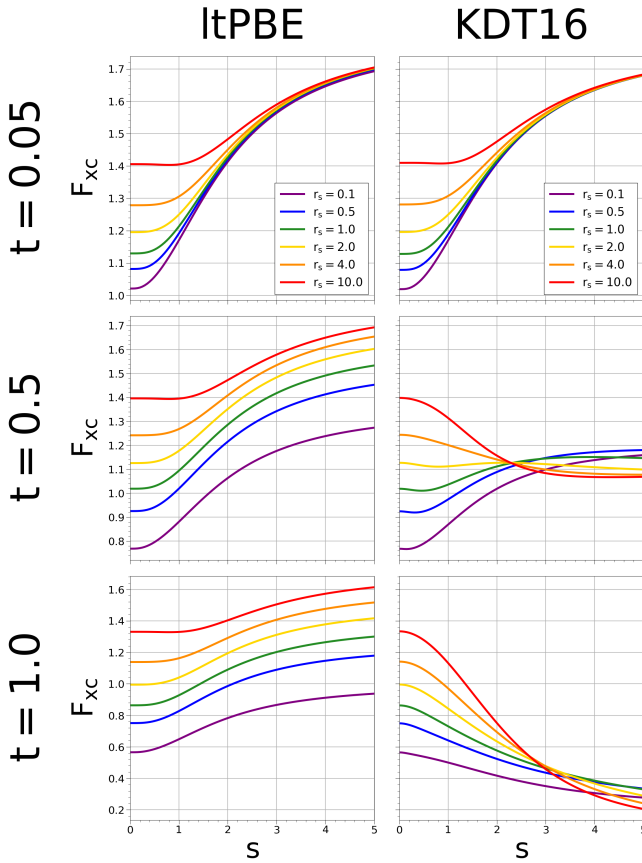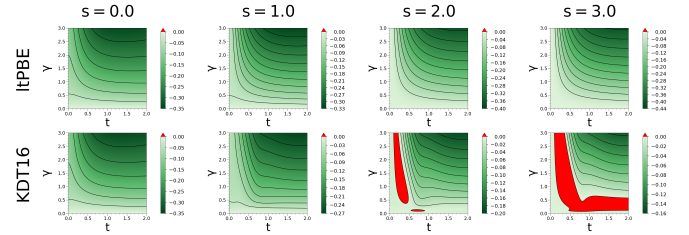
FIG. S5.   Temperature-dependent XC enhancement factors plotted as functions of the dimensionless gradient $s$ for unpolarized systems of various $r_{\mathrm{S}}$ values, with each row having a fixed reduced temperature $t$. The left column depicts the ltPBE approximation, while the right column depicts KDT16. The thermal coordinate scaling inequality mandates these curves not cross for any $t$.